doi:10.2533/chimia.2022.203 Chimia 76 (2022) 203–211

On-surface Synthesis: What Happens Behind the Scenes?

Samuel Stolz[a], Marco Di Giovannantonio[b], Oliver Gröning[c], and Roland Widmer*[c]

Abstract: On-surface synthesis has become a powerful approach to produce low-dimensional carbon-based nanostructures with atomistic precision. A large variety of analytical tools and methods are available to provide efficient monitoring of on-surface reactions, among which, scanning probe microscopy (SPM) has proven to be particularly efficient to characterize reaction intermediates and products down to the atomic scale. Nevertheless, due to limited temporal resolution, difficulties to explore the full temperature range, and lack of identifying the chemical environment of all elements involved in on-surface processes, SPM is ideally complemented with temperature programmed X-ray photoelectron spectroscopy (TP-XPS). In this short review, we aim to unveil some of the capabilities of synchrotron-based TP-XPS reporting on our own research on Ullmann-type on-surface coupling reactions.

Keywords: Dehalogenation · On-surface synthesis · Temperature programmed X-ray photoelectron spectroscopy

1. Introduction

The initial report of thermally activated dehalogenative aryl–aryl coupling on the well-defined, atomically flat single-crystalline gold surface under ultrahigh vacuum (UHV) conditions by Grill *et al.* in 2007,[1] provided the proof of concept for today's success of on-surface synthesis. This success stems from a reliable bottom-up approach to fabricate large, atomically precise molecular systems, whose structure can be controlled by appropriately designing the molecular precursors used as building blocks.[2–7] Moreover, on-surface synthesis circumvents several drawbacks of wet chemistry processes, such as the solubility problem particularly with regard to the products. Furthermore, because the synthesis takes place in UHV, the degradation of air-sensitive molecules is suppressed, and the occurrence of unwanted side reactions reduced, also due to the 2D templating effect of the substrate. The simplicity, reproducibility, and flexibility of on-surface synthesis resulted in the creation of numerous, and in many cases entirely new and long-sought-for, molecular structures, such as graphene nanoribbons (GNR) with controlled width and edge termination (Fig. 1),[8–12] magnetic nanographenes,[13–18] 1D organic spin chains,[19] or extended 2D organic networks.[20–22]

In this review article, we focus particularly on the investigation of dehalogenative aryl–aryl coupling, also referred to as Ullmann-type coupling, whose reaction process is illustrated in Fig. 1a,b, because it represents the most frequently encountered on-surface reaction scheme. Numerous other on-surface chemical reactions have been reported and are discussed in the reviews, *e.g.* from Shen *et al.*[5], Di Giovannantonio and Contini,[23] or Clair and Oteyza.[6] The initial step in the on-surface Ullmann-type coupling consists of the deposition of the precursor molecules on a metal surface in UHV, followed by a subsequent heating step to thermally activate the dehalogenative aryl–aryl coupling and thus the formation of covalent bonds between the precursor molecules. In some cases, an additional heating step is required to activate intramolecular cyclodehydrogenation to arrive at the targeted product.

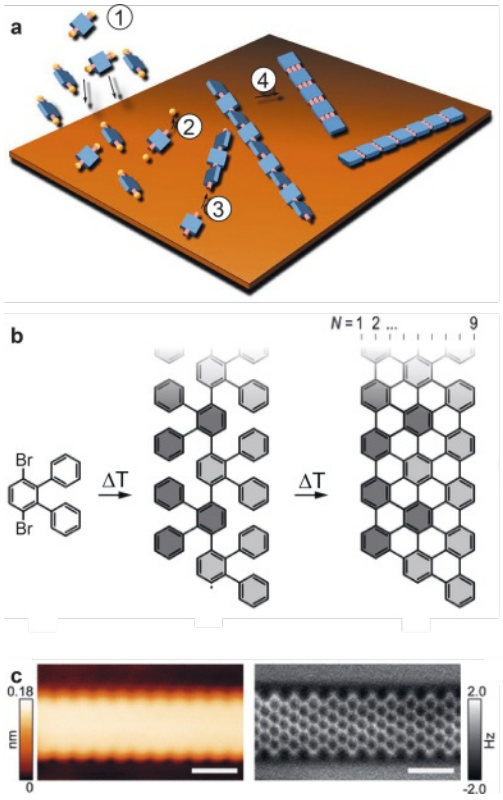

Fig. 1. a) Schematic illustration of on-surface GNR synthesis on Au(111) with (1) deposition of molecular precursors, (2) surface diffusion and elimination reaction of functional groups, (3) polymerization, and (4) cyclodehydrogenation. b) Reaction scheme for the on-surface synthesis of 9-AGNRs from (3',6'-dibromo-1,1':2',1''-terphenyl), on Au(111). c) STM and nc-AFM of a 9-AGNR segment (scale bar: 1 nm). (a) has been adapted from ref. [47], (b,c) with permission from ref. [48], copyright 2017 American Chemical Society.

*Correspondence: Dr. R. Widmer[c], roland.widmer@empa.ch

[a]Department of Physics, University of California, Berkeley, California 94720, United States; [b]Istituto di Struttura della Materia, CNR, Via Fosso del Cavaliere 100, I-00133 Roma, Italy; [c]Nanotech@surfaces Laboratory, Empa – Swiss Federal Laboratories for Materials Science and Technology, Überlandstrasse 129, CH-8600 Dübendorf, Switzerland

Creating extended molecular structures on metal surfaces ideally enables their investigation by surface science techniques such as scanning tunneling microscopy and spectroscopy (STM/S), which provide structural and electronic information of the nanoarchitectures with intramolecular resolution. In the case of non-contact atomic force microscopy (nc-AFM) with CO-functionalized tips[24,25] it is even possible to resolve intramolecular bonds (Fig. 1c). Although these scanning probe techniques have proven powerful[26] to identify the stable molecular structures for each reaction step,[6] they can neither identify the chemical environment of each element nor provide information about reaction kinetics due to poor temporal resolution and restricted temperature of operation. Therefore, the scanning probe techniques are commonly complemented with density functional theory (DFT) calculations, and from the experimental side, for instance with temperature programmed desorption (TPD)[27–29] or temperature programmed X-ray photoelectron spectroscopy (TP-XPS, previously also called fast-XPS).[29–46]

In TPD, desorbing species are detected by their mass during a controlled annealing of the sample. Therefore, TPD typically provides information on the kinetics of reactions in which the reaction products instantly desorb from the surface. On the other hand, TP-XPS accesses the chemical environment of each elemental species present at the surface by its core level shift according to the element's Madelung potential in a temperature-resolved manner.[49] Hence, when investigating a reaction, these two temperature-programmed techniques provide complementary insights, in particular, TPD regarding desorbing species and TP-XPS regarding the kinetics of surface confined reactions.

In TP-XPS, element-selected core-level spectra are continuously acquired to follow their evolution in time, mostly during a constant heating ramp, which correlates the temporal succession of the spectra with temperature. To achieve high temporal resolution, which translates to high-temperature resolution, synchrotron facilities in combination with display electron analyzers are particularly well suited. The former due to their high brilliance to enhance the signal to noise ratio and variable photon-energy to optimize the surface sensitivity, the latter due to its fast spectrum acquisition. A representative dataset of a TP-XPS measurement is shown in Fig. 2. The TP-XPS map of the Br 3d core level in Fig. 2a monitors the on-surface dehalogenation process of bromine detaching from 5-bromo-7-methylbenz(a)anthracene (BMA), its transitory chemisorbed state on the gold substrate and finally its desorption.[43] Each of the roughly 200 horizontal lines of the TP-XPS intensity map corresponds to an individual XPS spectrum of the Br 3d core level doublet (Br $3d_{5/2}$ and Br $3d_{3/2}$) with a temperature resolution of about 2 K. Starting with the pristine molecule from below 200 K, we observe that around 350 K, the Br 3d doublet shifts within a relatively narrow temperature range by about 2 eV to lower binding energy (BE) before the overall intensity of the doublet decreases above about 420 K. The shift to lower BE is a result of the detachment of bromine from the molecule and its subsequent chemisorption on the Au(111) surface. The decrease of the overall intensity of the Br 3d doublet corresponds to desorption of the bromine atoms. In Fig. 2b, representative line profiles of the TP-XPS map in Fig. 2a are extracted to show the Br 3d doublet for each of the three different states.

Although there are several studies using TP-XPS, we will illustrate its capabilities based on investigations of our research group, which all have been carried out at the PEARL endstation[50] of the synchrotron facility at the Paul Scherrer Institute in Switzerland.

We will first discuss how TP-XPS evidenced the reversibility of the halogen elimination process in the on-surface dehalogenative aryl–aryl coupling on Au(111).[42] As a second illustration of the method, we will review the impact of the halogen type in the precursor molecule[29] or the precursor molecules' coverage[45] on the GNR length, which enabled the successful integration of small band-gap GNR in a field effect transistor. Finally, we discuss the potential of TP-XPS to determine kinetic information for asymmetric on-surface reactions.[43]

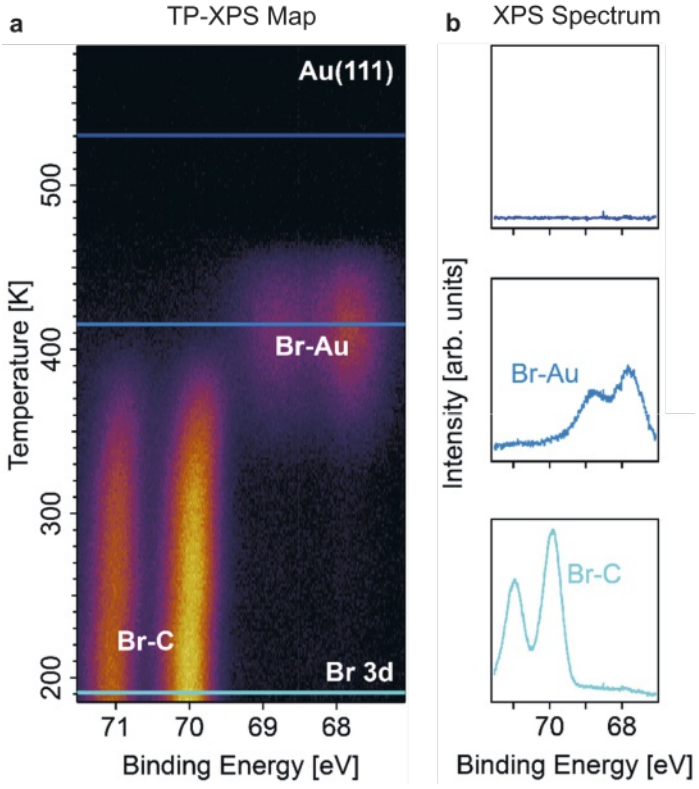

Fig. 2. a) TP-XPS map of the Br 3d core level doublet during a heating ramp of 0.1 $K \cdot s^{-1}$ of BMA on Au(111). b) Horizontal profiles extracted from a at specific temperatures. Figure adapted from ref. [43].

2. Reversibility of On-surface Chemical Reactions

Even though the first experimental study of thermally induced on-surface dehalogenative aryl–aryl coupling dates back to 2007, the combination of STM, nc-AFM and XPS investigations could so far only establish the nature of the thermodynamically stable states along the reaction pathway.[42] On Au(111), the halogen elimination and carbon–carbon bond formation processes usually occur simultaneously,[28,30,31] hence no intermediate molecular species are observed. In contrast on Cu(111), the halogen elimination occurs at lower temperatures as the carbon–carbon bond formation.[31,33,51,52] Therefore, the formation of an organometallic (OM) phase in which the dehalogenated molecules bind with the radical site to copper adatoms is commonly observed. Although TP-XPS experiments have been conducted to gain further insight into the reaction pathway, the determination of the corresponding energetics has only be determined for a limited number of cases by using the Polanyi-Wigner equation, which is commonly applied for the analysis of the desorption kinetics in TPD experiments.

One implicit assumption connected to the Polanyi-Wigner equations is the irreversibility of the reaction process, which is not evident for on-surface reactions and should be explicitly clarified by experiment. In particular, assuming that the halogen elimination process is reversible instead of irreversible, it should then be possible to passivate the dehalogenated carbon site with another, stronger bound halogen species.[53] Consequently, we investigated the reversibility of the dehalogenation process by checking with TP-XPS whether the bromine atoms of the prototypical 4,4''-dibromo-*p*-terphenyl (DBPTP), which polymerizes into poly(*para*-phenylene) (PPP), could be exchanged by chlorine atoms on the Au(111) and Cu(111) surfaces (Fig. 3, Fig. 4).

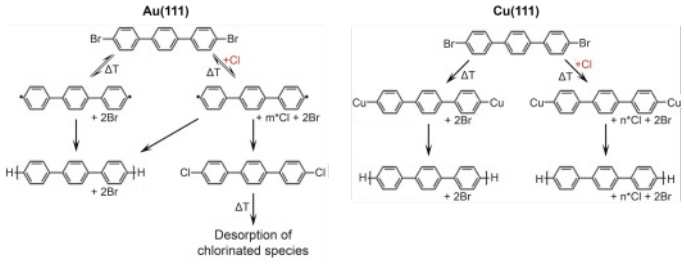

Fig. 3. Reaction overview of DBPTP polymerization on Au(111) and Cu(111). Adapted with permission from ref. [42], licensed by Wiley VCH.

As seen in the temperature dependence of the Cl 2p core level doublet for the reaction on Au(111) in Fig. 4b, there is a distinct shift of some intensity to higher BE starting around 400 K (indicated with a white circle in Fig. 4b), which coincides with a shift to lower BE in the Br 3d doublet in Fig. 4a. The shift in the Br 3d doublet corresponds to the detachment of bromine from the molecules, while the shift in the Cl 2p doublet to higher BE can be attributed to the formation of covalent carbon–chlorine bonds. Since the two processes coincide in temperature – which is best seen by extracting the relative intensity curves, further referred to as kinetic curves, of each chemical state of the halogens shown in Fig. 4c – we have strong evidence that chlorine binds to the debrominated carbon site of the DBPTP molecule and thus that the dehalogenation process is reversible on Au(111). On the other hand, when performing the same experiment on Cu(111), we observe no chemical shift in the Cl 2p doublet over the whole investigated temperature range (Fig. 4d,f), indicating the dehalogenation to be irreversible due to the formation of stable OM intermediates.

The reaction scheme for the dehalogenative aryl–aryl coupling including a reversible halogen elimination process reads (Eqn. (1)):

$$\begin{cases} A \underset{k_{-1}}{\overset{k_1}{\rightleftarrows}} B + X \\ 2B \xrightarrow{k_2} C \end{cases} \quad (1)$$

where A, B, X and C are the amount of precursor molecules (*i.e.* DBPTP), of debrominated molecules, of halogen atoms chemisorbed on the surface and of covalently coupled molecular products (*i.e.* PPP), respectively, while k_1, k_{-1}, and k_2 are the kinetic constants for dehalogenation, re-halogenation and polymerization. The kinetic constants are assumed to be of the form $k_i = \nu \cdot e^{\frac{\Delta E_i}{k_B T}}$ where ν is the attempt frequency (set to $10^{13}\,s^{-1}$), ΔE_i is the activation energy of the process, k_B is the Boltzmann constant, and T is the temperature.

This aforementioned reaction pathway is described by the following set of differential equations (Eqn. (2)):

$$\begin{cases} \frac{d[A]}{dt} = -k_1[A] + k_{-1}[B][X] \\ \frac{d[B]}{dt} = k_1[A] - k_{-1}[B][X] - k_2[B]^2 \\ \frac{d[X]}{dt} = k_1[A] - k_{-1}[B][X] \\ \frac{d[C]}{dt} = k_2[B]^2 \end{cases} \quad (2)$$

As our experiments were performed with a constant heating rate α, the derivative with respect to time *t* can be replaced by the one with respect to temperature T: $\frac{d}{dt} = \frac{1}{\alpha}\frac{d}{dT}$. When fitting the experimentally determined kinetic curves for all chemical environments of the bromine and carbon atoms for the dehalogenative aryl–aryl coupling of DBPTP on Au(111) (Fig. 5a) with the whole set of equations, we can experimentally determine the energetics of the whole reaction path (Fig. 5b). We find energy barriers of 0.95 eV, 0.67 eV, and 0.70 eV for the debromination, re-bromination and polymerization process, respectively. Importantly, fitting the kinetic curves without taking into account the reversibility of dehalogenation step fails to reproduce the experimental data.

In the case of DBPTP/Cu(111), the intermediate corresponds to an OM compound, which is energetically more stable than pristine DBPTP adsorbed on Cu(111). Hence the kinetic constant for re-bromination k_{-1} becomes negligibly small, reducing the rate equations to (Eqn. (3)):

$$\begin{cases} \frac{d[A]}{dt} = -k_1[A] \\ \frac{d[B]}{dt} = k_1[A] - k_2[B]^2 \\ \frac{d[X]}{dt} = k_1[A] \\ \frac{d[C]}{dt} = k_2[B]^2 \end{cases} \quad (3)$$

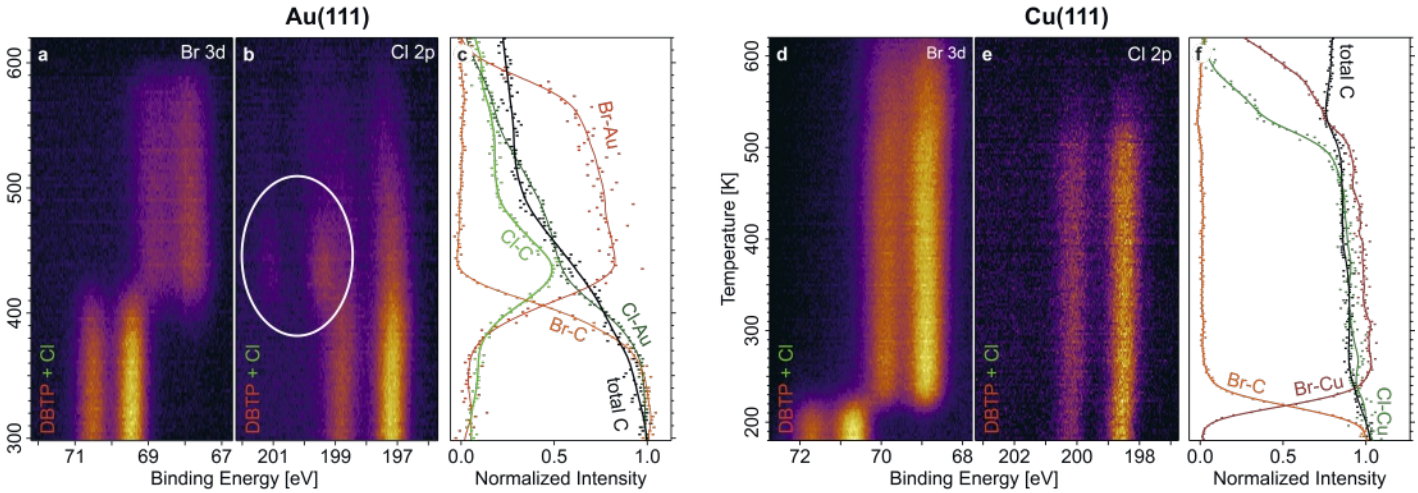

Fig. 4. Temperature evolution of DBPTP + Cl on (a–c) Au(111) and (d–f) Cu(111). TP-XPS maps of Br 3d (a,d) and Cl 2p (b,e) doublets during the annealing of DBPTP + Cl on the respective metal surface. Temperature dependence for all chemical states of Cl and Br, together with the total carbon coverage (c,f). The trend of each experimental curve (dots) is indicated with a spline (solid line). Adapted with permission from ref. [42], licensed by Wiley VCH.

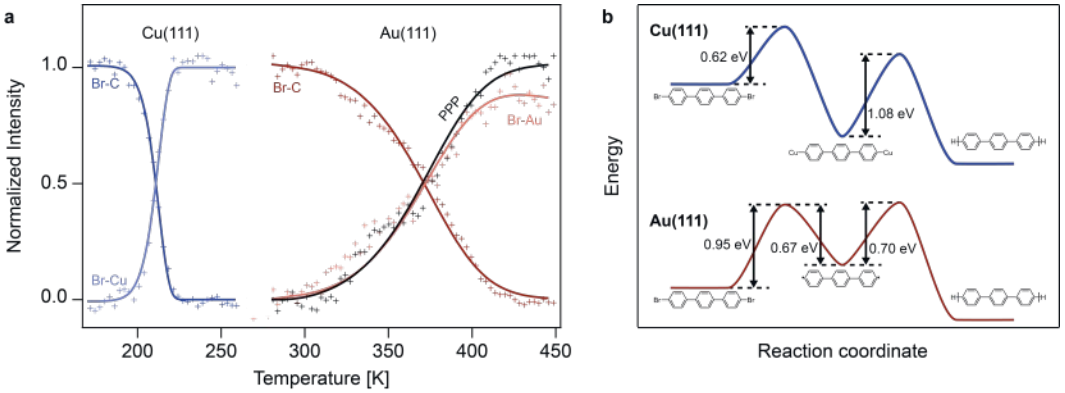

Fig. 5. a) Temperature evolution of Br–C, Br-metal and PPP normalized signals extracted from the TP-XPS maps (markers) and fitted with the kinetic models for Cu(111) and Au(111) described in the text (solid lines). b) Experimentally derived energy profiles for the PPP formation from DBPTP on the two substrates. The energy barriers have been obtained by fitting the kinetic curves in (a). Adapted with permission from ref. [42], licensed by Wiley VCH.

The first of these equations describes the irreversible DBPTP debromination and corresponds to the Polanyi-Wigner equation for a first-order reaction, while the fourth equation, depicting the polymerization, is a Polanyi-Wigner equation for a second-order reaction. As the debromination and polymerization processes are well separated in temperature, they can be analyzed independently. The successful fitting of experimental data (Fig. 5a) results in a debromination energy barrier of 0.62 eV and polymerization energy barrier of 1.08 eV for Cu(111) (Fig. 5b). The experimentally determined energy barriers are in good agreement with those estimated using DFT[36,54] calculations for the dehalogenative aryl–aryl coupling of DBPTP on both Au(111) and Cu(111).

Such insight into a widely exploited on-surface dehalogenative aryl–aryl coupling is a prerequisite for improving its efficiency and selectivity. In particular, on Au(111), the rate-limiting step for this polymerization reaction is the breaking of carbon–bromine bonds. By choosing molecular precursors with weaker bonded halogens, the dehalogenation process occurs at lower temperatures, thus decreasing the likelihood of unwanted side-reactions.[29] As discussed in the next chapter, exchanging bromine with iodine in the precursor molecule has accordingly a profound effect on the length distribution of 1D-polymers.

3. Controlling the Length of 1D-polymers by Optimizing the Halogen Functionalization

The impact of exchanging bromine with iodine in the precursor molecule is exemplarily illustrated for the synthesis of 9-armchair GNR (9-AGNRs, see Fig. 1 for the reaction scheme) in Fig. 6.[29] STM investigations revealed that the usage of iodinated (3',6'-diiodo-1,1':2',1''-terphenyl (DITP)) instead of brominated (3',6'-dibromo-1,1':2',1''-terphenyl (DBTP, Fig. 1b)[48]) precursor molecule lowers the polymerization temperature and triples the average length of the formed 9-AGNRs from 15 nm to 45 nm (Fig. 6c). In this context, increasing the length of 1D-polymers is of profound technological relevance, as it allows a more efficient and reliable bridging of the electronic contacts in devices.[55]

To shed light onto the detailed mechanism leading to longer 9-AGNRs for DITP than for DBTP, we monitored the temperature evolution of the C 1s and the respective halogen core level by TP-XPS – the results are presented in Fig. 7. Extracted from the TP-XPS maps (Fig. 7c–f), Fig. 7b displays the total intensities of the halogen and carbon core levels as a function of temperature. Fig. 7g shows the normalized intensities of each chemical state of the halogen and the molecular backbone for DITP/Au(111). In a first step, we focus on the dehalogenation process, which is associated to the shift towards lower BE of the halogen doublets and a corresponding shift to lower BE in the C 1s core level. As expected from the previous discussion, the halogen detachment process occurs at significantly lower temperatures for DITP as compared to DBTP, namely around 350 K instead of 440 K. For both precursor molecules, the halogen detachment process is the rate-limiting step, because for both systems individually, the processes of halogen detachment and aryl–aryl coupling proceed over the same temperature range.

The difference in halogen elimination temperature for DITP and DBTP has profound consequences. Unlike DITP, a large number of DBTP molecules desorb rather than debrominate, as evidenced by the strong decrease in the integrated C 1s and Br 3d core level intensities shown in Fig. 7b. Moreover, for DITP the halogen elimination process is farther separated in temperature from the cyclodehydrogenation process (expressed as a shift in the C 1s core level of about 0.3 eV to higher BE in Fig. 7e,f), which planarizes the polymers and is initiated above 550 K for both precursor molecules. According to the hypothesis that the length of the polymers is limited due to passivation of the reactive carbon site by atomic hydrogens released during the cyclodehydrogenation process, a larger temperature separation of the halogen detachment and cyclodehydrogenation, controlled by the choice of the halogen species in the precursor molecule, results in significantly longer 9-AGNRs.

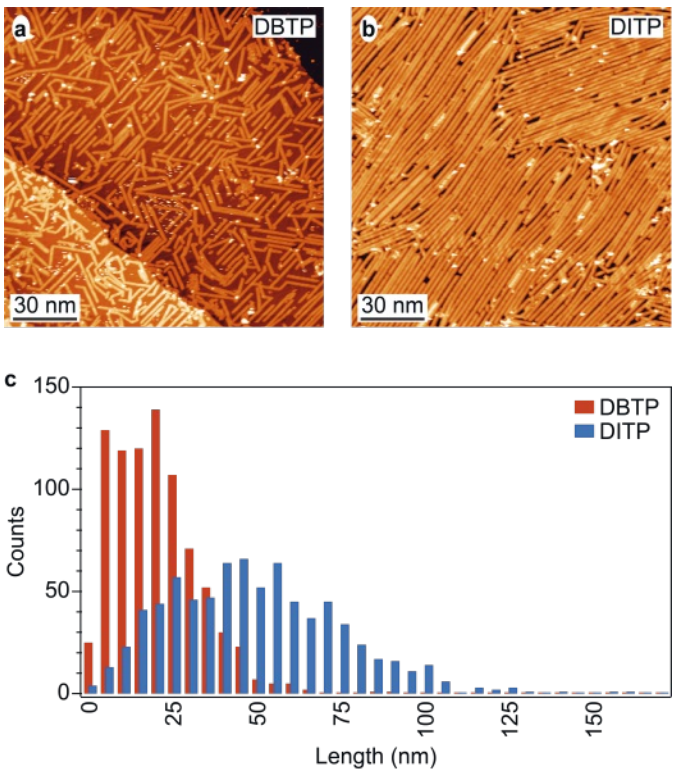

Fig. 6. STM images showing the different length of 9-AGNRs obtained from DBTP (a) and DITP (b). The histograms in (c) report the length distribution determined for the two systems using large-scale STM images. Adapted with permission from ref. [29], copyright 2018 American Chemical Society.

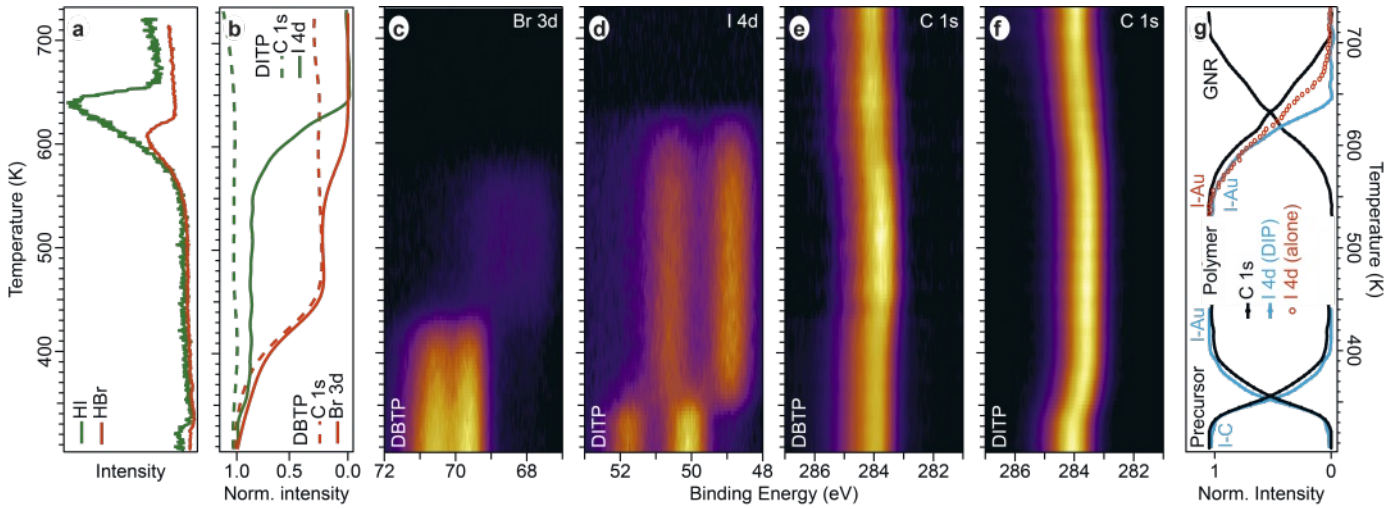

Fig. 7. a) TPD curves showing the desorption rates of HBr and HI as a function of increasing temperature (heating rate of 1 $K \cdot s^{-1}$). b) Normalized total area of each horizontal profile of the TP-XPS maps. c–f) TP-XPS maps of Br 3d, I 4d, and C 1s recorded during the annealing (heating rate of 0.2 $K \cdot s^{-1}$) of the Au(111) surface after deposition of DBTP (c,e) or DITP (d,f) at 300 K. Because of DBTP desorption upon annealing, the map in (e) has been normalized by the total area to highlight the energy shift. g) Kinetic curves extracted from the C 1s (black) and I 4d (cyan) TP-XPS maps of DITP. The maximum intensity of each signal corresponds to the fraction of elements in the appropriate chemical environment and has been normalized to 1. The kinetic curve for the desorption of iodine alone is shown for comparison (red empty circles). Adapted with permission from ref. [29], copyright 2018 American Chemical Society.

In addition to the insights into the length dependence, the evolution of the kinetic profiles shown in Fig. 7g represent a valuable tool to quantitatively analyze reaction mechanisms. Here, we can relate the dehalogenation and concurrent polymerization processes to second-order kinetics with onset of 320 K and activation energy of about 1.0 eV, assuming a pre-exponential factor (attempt frequency) of 10^{13} s^{-1}. On the other hand, the more complex kinetic curves for the cyclodehydrogenation process could be fitted with linear combination of Polanyi-Wigner equations, but a proper interpretation requires extensive additional experimental and theoretical investigation to settle the reaction mechanism.[56,57]

4. Controlling the Length of 1D-polymers with the Precursor Coverage

Interestingly, for the synthesis of 9-AGNRs, the onset of the cyclodehydrogenation process coincides with the onset for the halogen desorption. According to TPD experiments (Fig. 7a), the halogens desorb as XH, X = {Br,I}, hence the halogen atoms seem to act as drain for the atomic hydrogen created during cyclodehydrogenation. Abyazisani *et al.*[58] reported a similar observation, namely that they could remove halogens created during the dehalogenative aryl–aryl coupling by exposing the metal surface to atomic hydrogen. As outlined in the following, we relate the significant increase of average 5-AGNR length when using molecular precursor coverages exceeding 1 monolayer (ML) to a depletion of atomic hydrogen by the increased amount of atomic iodine available on the surface.[45]

In Fig. 8, we present STM investigations of the synthesis of 5-AGNRs[44,59] grown from low (0.9 ML, Fig. 8b) and high (1.5 ML, Fig. 8c) initial diiodo-perylene (DIP, Fig. 8a) coverage on Au(111). Based on the STM images in Fig. 8b,c, we could determine the 5-AGNR length distribution for the two cases, as presented in the histogram in Fig. 8d. The length of 5-AGNRs is limited to a few nanometers for the low coverage case but increases to about 17 nm for the high coverage case.

To explore the origin of this very pronounced dependence of the average 5-AGNR length on the initial precursor coverage, we again performed TP-XPS, the results of which are summarized in Fig. 9. As evidenced by the temperature evolution of the I 4d doublet (Fig. 9a,d) and the shift of the C 1s core level (Fig. 9b,e), the molecular precursor coverage has a minor effect on the halogen elimination temperature. On the other hand, the temperature window in which iodine desorbs strongly depends on the initial DIP coverage. Iodine desorption occurs between 580 K and 650 K and between 430 K and 590 K for low and high coverage, respectively (Fig. 9c,f). Interestingly, the desorption kinetics in the low coverage case is very similar to the desorption of iodine alone, *i.e.* without the presence of concomitant cyclodehydrogenation and the associated release of hydrogen.

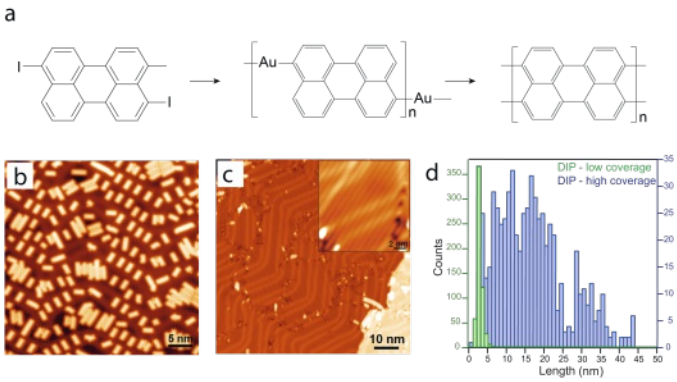

Fig. 8. a) Molecular precursor and reaction pathway for the on-surface synthesis of 5-AGNRs on Au(111). STM image of 5-AGNRs synthesized from low (b) and high (c) initial precursor molecule coverage resulting in a length distribution presented in the histogram in (d). Adapted from ref. [45].

The temperature evolution of the C 1s core level exhibits a strong shift to low BE after the halogen elimination process, which is attributed to the formation of an OM phase, as also observed by Berdonces-Layunta *et al.*[44] As seen in Fig. 9c,f, the temperature dependence of the relative intensity of the OM phase, which is transformed into 5-AGNRs by simultaneous polymerization and cyclodehydrogenation, strongly depends on the initial DIP coverage. Specifically, the intensity of the OM phase decreases between 390 K and 470 K and between 430 K and 590 K for low and high initial DIP coverage, respectively. While the temperature ranges for the OM depletion and iodine desorption are well separated by 190 K in temperature for low initial DIP coverage, they occur over nearly the same temperature range for high initial DIP coverage. This suggests that for high

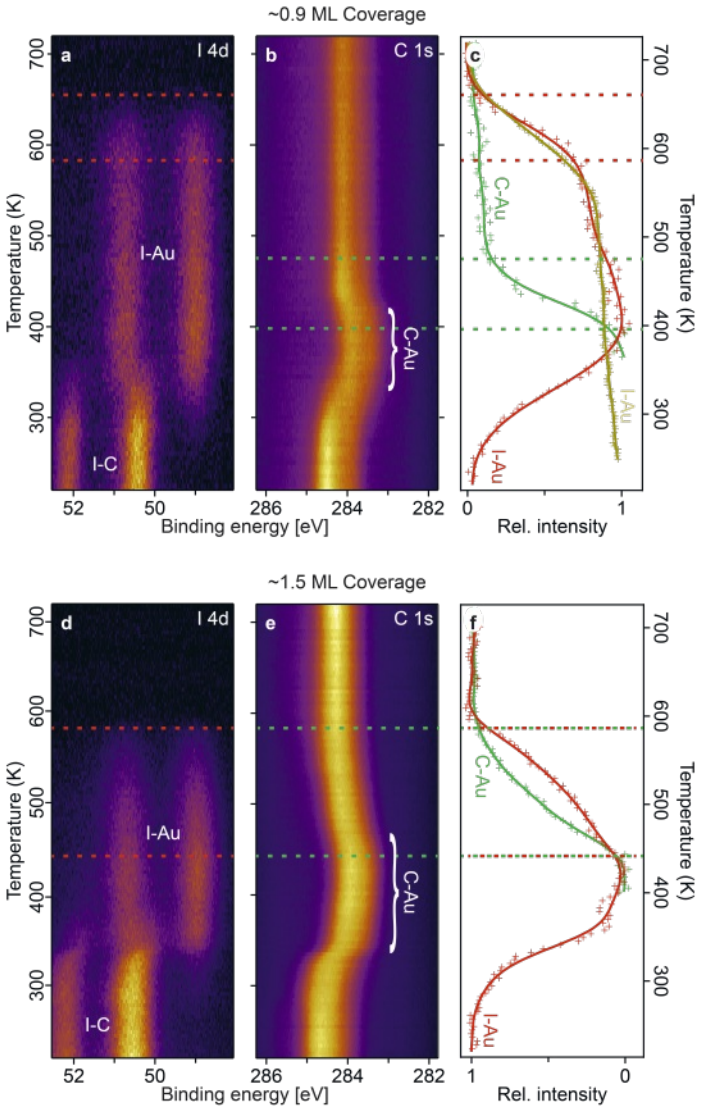

Fig. 9. TP-XPS maps of I 4d and C 1s core levels recorded during the heating (rate of 0.2 $K \cdot s^{-1}$) of the low (~0.9 ML) (a,b) and high (~1.5 ML) (d,e) DIP coverage samples. The maps with high precursor coverage in (d,e) are normalized by the total area to highlight the energy shift. c,f) Kinetic curves showing the temperature evolution of the OM phase and chemisorbed iodine. The kinetic curve of pure iodine on Au(111) in (c) is included for comparison (yellow curve, from ref. [29]). The markers in (c,f) are the experimental data, and the solid line is a spline and serves as guide for the eye. Adapted from ref. [45].

initial DIP coverage, the iodine desorption and GNR formation are inherently connected. Based on the TPD results for 9-AGNRs in Fig. 7a, iodine atoms might act as trap for atomic hydrogen, which reduces unwanted passivation of the dehalogenated carbon sites by atomic hydrogen in the growing 5-AGNRs. As one can imagine, the efficiency of such a trapping process can be strongly dependent on the availability and proximity of iodine atoms and thus on the initial coverage of the precursor molecules.

Only thanks to the increased length, 5-AGNRs could be successfully integrated into field-effect switching devices that can be operated at room temperature by bridging Pd electrodes and in the present case showed on-off ratios of up to 10^3 and on-currents of up to 0.4 µA.[45]

5. Enantioselective Dehalogenation

Recently, we have extended the scope of TP-XPS investigations from symmetric on-surface reactions (like the GNR synthesis) to asymmetric ones. Asymmetric synthesis, which contrasts the resolution of racemic mixtures, has become of paramount importance, especially in pharmaceutical, agricultural, or food industry.[60,61] In this context, the application of chiral heterogeneous catalysts promise increased stability and facilitated separation and recycling, but remained largely unexplored. Here, we employ prototypical, chiral, intermetallic PdGa{111} surfaces[43] for the investigation of an asymmetric halogen elimination reaction. Owing to its non-centrosymmetry, PdGa exists in two enantiomorphs that are denoted PdGa:A and PdGa:B.[62,63] Of particular interest are the two structurally inequivalent, threefold symmetric, chiral PdGa:A$(\bar{1}\bar{1}\bar{1})$Pd$_3$ and PdGa:A(111)Pd$_1$ surfaces (denoted as A:Pd$_3$ and A:Pd$_1$, respectively), which terminate by Pd trimers and isolated single Pd atoms, respectively. Specifically, for prochiral BMA (Fig. 10a) we demonstrate the enantioselective debromination, which as described above, is the first step not only in Ullmann-type aryl–aryl coupling,[6] but also for several other on-surface reactions.[64–66] BMA is deposited on the A:Pd$_3$, A:Pd$_1$ and as a reference substrate on Au(111), and appears as racemic mixture (of its prochiral surface enantiomers S and R) on all three surfaces in its pristine form, as evidenced by SPM (Fig. 10b,c).

Upon annealing to 250 K, we observe by SPM that only one of the two BMA surface enantiomers remains pristine, while all the opposite S(R) surface enantiomers debrominate on A:Pd$_3$(A:Pd$_1$) (Fig. 10b,c). Interestingly, the sequence of debromination for the two surface enantiomers is reversed between A:Pd$_3$ and A:Pd$_1$. Again, SPM cannot deliver detailed information on the enantiospecific reaction kinetics, thus we performed TP-XPS (*cf.* Fig. 10d–g). The kinetic curves assigned to bromine bonded to the molecule (Br–C) and bromine adsorbed on the surface (Br–M, M={Au,Pd}) are shown in Fig. 10g for all three surfaces. The decrease of the Br–C intensity, which corresponds to debromination of BMA occurs between 300 K and 400 K on Au(111), but already takes place between 200 K and 290 K and between 200 K and 300 K for the Pd$_3$- and Pd$_1$-terminated PdGa{111} surfaces, respectively.

Closer inspection of the Br–C kinetic curves for the three surfaces reveals that they not only decrease in a dissimilar temperature range, but also exhibit different line shapes. In particular, the Br–C signal declines in a sigmoidal, linear, and double-sigmoidal shape for Au(111), A:Pd$_3$, and A:Pd$_1$, respectively. This behavior is investigated in more detail by describing the debromination kinetics more quantitatively by assuming the reaction scheme shown in Fig. 11 and applying the resulting rate equations in Eqn. (4) to calculate the energy barriers.

$$\begin{cases} \frac{d[Ed_X]}{dT} = -\frac{1}{\alpha}(k_{1_X}[Ed_X] + k_{-1_X}[Br][Int_X]) \\ \frac{d[Br]}{dT} = \frac{1}{\alpha}(k_{1_X}[Ed_X] - k_{-1_X}[Br][Int_X]) \\ \frac{d[Int_X]}{dT} = \frac{1}{\alpha}(k_{1_X}[Ed_X] - k_{-1_X}[Br][Int_X] - k_{2_X}[Int_X]^2) \\ \frac{d[P_X]}{dT} = \frac{1}{\alpha}(k_{2_X}[Int_X]^2) \end{cases} \quad (4)$$

The subscript X represents the two surface enantiomeric forms of BMA, thus taking into account the possibility of enantiospecific reaction pathways. While the Br–C signal obtained for BMA on Au(111) could be fit with Eqn. (2), *i.e.* without assuming enantiospecific reaction kinetics, we had to include enantiospecific reaction pathways to achieve a reasonable match for the Br–C signal for BMA on A:Pd$_3$ and A:Pd$_1$. In Eqn. (4), we assume the reaction to be enantioselective because of different debromination energies of the BMA enantiomers, *i.e.* $k_{1S} \neq k_{1R}$; $k_{-1S} = k_{-1R}$; $k_{2R} = k_{2S}$, which is illustrated in Fig. 11b. From the fitting of the TP-XPS data in Fig. 10g with Eqn. (4), we could determine the mean debromination temperatures for each BMA surface enantiomer to be $T_{DebR} = T_{DebS} = 367$ K for Au(111), $T_{DebR} = 258$ K and $T_{DebS} = 219$ K for A:Pd$_3$, and $T_{DebR} = 228$ K and $T_{DebS} = 275$ K for A:Pd$_1$. Moreover, for the enantiospecific reaction paths in Fig. 11b, we

determined the energy barrier differences for the debromination of the BMA surface enantiomers of 0 meV, 40 meV, and 55 meV on Au(111), A:Pd_3, and A:Pd_1, respectively.Based on the TP-XPS results, we could demonstrate the enantiospecific halogen elimination process of prochiral BMA with unprecedentedly high differences in debromination temperatures of the two surface enantiomers of 36 K and even 46 K on the Pd_3- and Pd_1-terminated PdGa{111} surfaces, respectively. Moreover, the observation that on Pd_3- and Pd_1-terminated PdGa{111} surfaces of the same enantiomorph the opposite BMA surface enantiomer debrominates at lower temperatures (*cf.* Fig 10b,c) evidences a strong geometrical ensemble effect[67] due to the different surface atomic arrangement between Pd_1 and Pd_3, and emphasizes the significance of the atomic details of the entire molecule-substrate system.

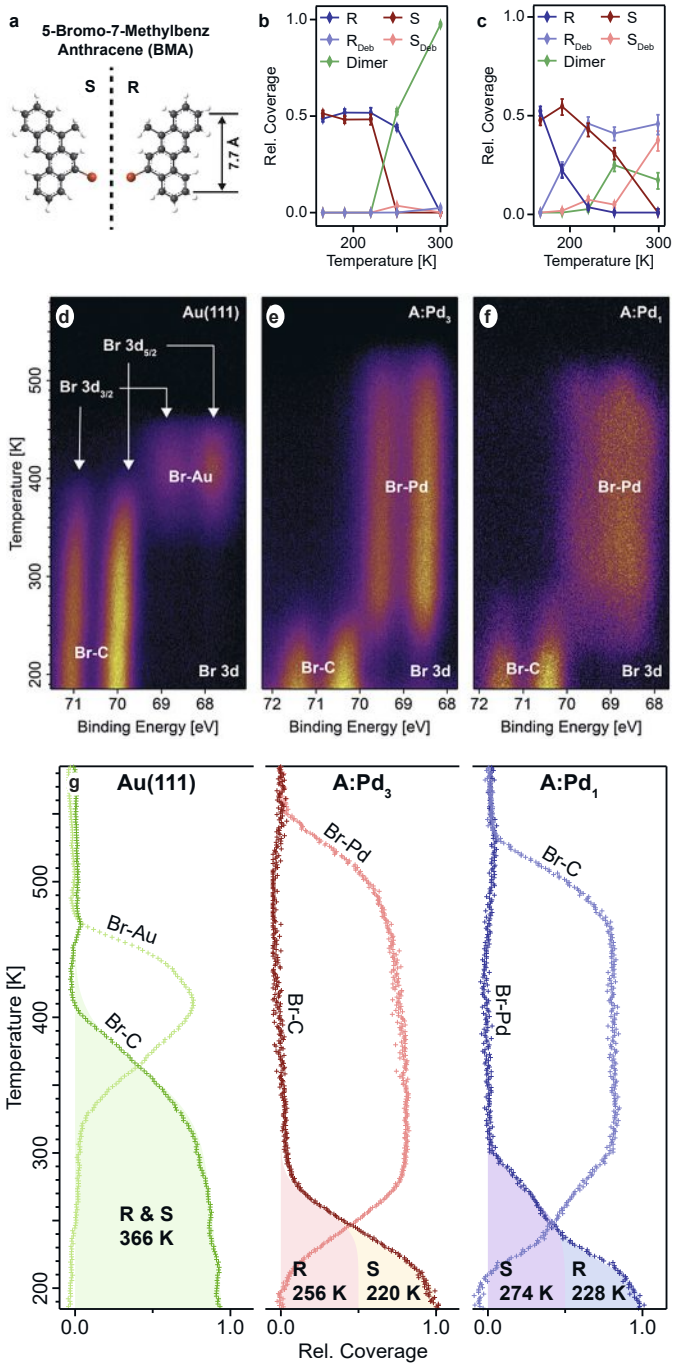

Fig. 10. a) Molecular structure of BMA. Temperature evolution of the BMA surface enantiomers on PdGa:A($\bar{1}\bar{1}\bar{1}$)Pd_3 (b) and PdGa:A(111) Pd_1 (c) determined from SPM experiments. TP-XPS maps of the Br 3d core level doublet for BMA adsorbed on Au(111) (d), PdGa:A($\bar{1}\bar{1}\bar{1}$)Pd_3 (e) and PdGa:A(111)Pd_1 (f). g) Temperature dependence of the Br–C and Br–Au/Br–Pd components extracted from the Br 3d TP-XPS maps and normalized to the initial bromine signal. The shaded areas beneath each curve show fits with Eqn. (4); the contribution of each BMA surface enantiomer, with the enantiomeric form as determined from SPM, is displayed in a different color. The temperatures at which half of the respective surface enantiomer is debrominated are given in the legend. Adapted from ref. [43].

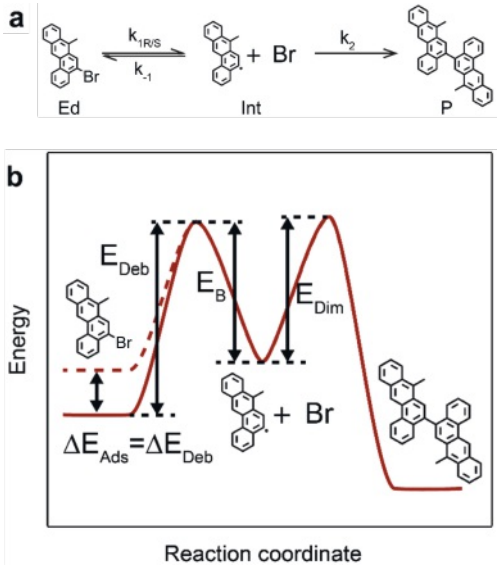

Fig. 11. a) Reaction scheme with educt (Ed), intermediate (Int) and product (P). b) Asymmetric reaction pathway assumed for the determination of the energy barriers from the temperature-dependent relative XPS intensities in Fig. 10g. Adapted from ref. [43].

6. Conclusion

Based on the selected examples presented in this topical short review, we conclude that TP-XPS offers valuable information on the reaction kinetics and unique insights into on-surface reaction mechanisms. In particular, the energy barriers of several reaction steps can be determined, which allows the identification of the rate-limiting step and sets the basis to optimize the reaction path. It needs to be emphasized that TP-XPS is neither restricted to the presented dehalogenative aryl–aryl coupling nor to thermally induced reactions but could be applied to any on-surface reaction initiated by various stimuli, or just occurring over time. In general, the combination of SPM techniques providing information with high spatial resolution and TP-XPS to obtain significant thermal resolution is highly complementary and allows unprecedented understanding of complex on-surface processes. With the PEARL beamline at the Swiss Light Source at PSI, the Swiss and the international research communities has an excellent instrument at their disposal to perform high resolution TP-XPS for the elucidation of surface-confined reactions.

Acknowledgements

The authors acknowledge funding from the Swiss National Science Foundation under SNSF Project No. 195133, the US Office of Naval Research BRC Program, the European Commission Graphene Flagship (no. CNECT-ICT-604391), and the Max Planck Society. The XPS experiments were performed with assistance of Matthias Muntwiler on the X03DA (PEARL) beamline at the Swiss Light Source, Paul Scherrer Institut, Villigen, Switzerland. We acknowledge all members of the nanotech@surfaces laboratory for their contribution to the sophisticated experiments.

Received: December 15, 2021

[1] L. Grill, M. Dyer, L. Lafferentz, M. Persson, M. V. Peters, S. Hecht, *Nat. Nanotechnol*. **2007**, *2*, 687, https://doi.org/10.1038/nnano.2007.346.
[2] N. R. Champness, *Nat. Nanotechnol*. **2007**, *2*, 671, https://doi.org/10.1038/nnano.2007.355.
[3] J. A. Martin-Gago, *Nat. Chem*. **2011**, *3*, 11, https://doi.org/10.1038/nchem.923.
[4] G. Franc, A. Gourdon, *Phys. Chem. Chem. Phys*. **2011**, *13*, 14283, https://doi.org/10.1039/c1cp20700h.
[5] Q. Shen, H.-Y. Gao, H. Fuchs, *Nano Today* **2017**, *13*, 77, https://doi.org/10.1016/j.nantod.2017.02.007.
[6] S. Clair, D. G. de Oteyza, *Chem. Rev*. **2019**, *119*, 4717, https://doi.org/10.1021/acs.chemrev.8b00601.
[7] S. Song, J. Su, M. Telychko, J. Li, G. Li, Y. Li, C. Su, J. Wu, J. Lu, *Chem. Soc. Rev*. **2021**, *50*, 3238, https://doi.org/10.1039/D0CS01060J.
[8] J. Cai, P. Ruffieux, R. Jaafar, M. Bieri, T. Braun, S. Blankenburg, M. Muoth, A. P. Seitsonen, M. Saleh, X. Feng, K. Müllen, R. Fasel, *Nature* **2010**, *466*, 470, https://doi.org/10.1038/nature09211.
[9] C. Sánchez-Sánchez, T. Dienel, O. Deniz, P. Ruffieux, R. Berger, X. Feng, K. Müllen, R. Fasel, *ACS Nano* **2016**, *10*, 8006, https://doi.org/10.1021/acsnano.6b04025.
[10] P. Ruffieux, S. Wang, B. Yang, C. Sánchez-Sánchez, J. Liu, T. Dienel, L. Talirz, P. Shinde, C. A. Pignedoli, D. Passerone, T. Dumslaff, X. Feng, K. Müllen, R. Fasel, *Nature* **2016**, *531*, 489, https://doi.org/10.1038/nature17151.
[11] O. Gröning, S. Wang, X. Yao, C. A. Pignedoli, G. Borin Barin, C. Daniels, A. Cupo, V. Meunier, X. Feng, A. Narita, K. Mullen, P. Ruffieux, R. Fasel, *Nature* **2018**, *560*, 209, https://doi.org/10.1038/s41586-018-0375-9.
[12] D. J. Rizzo, G. Veber, T. Cao, C. Bronner, T. Chen, F. Zhao, H. Rodriguez, S. G. Louie, M. F. Crommie, F. R. Fischer, *Nature* **2018**, *560*, 204, https://doi.org/10.1038/s41586-018-0376-8.
[13] J. Su, M. Telychko, P. Hu, G. Macam, P. Mutombo, H. Zhang, Y. Bao, F. Cheng, Z.-Q. Huang, Z. Qiu, S. J. R. Tan, H. Lin, P. Jelínek, F.-C. Chuang, J. Wu, J. Lu, *Sci. Adv.* **2019**, *5*, eaav7717, https://doi.org/10.1126/sciadv.aav7717.
[14] S. Mishra, D. Beyer, K. Eimre, S. Kezilebieke, R. Berger, O. Gröning, C. A. Pignedoli, K. Müllen, P. Liljeroth, P. Ruffieux, X. Feng, R. Fasel, *Nat. Nanotechnol*. **2019**, *1*, https://doi.org/10.1038/s41565-019-0577-9.
[15] S. Mishra, D. Beyer, K. Eimre, J. Liu, R. Berger, O. Gröning, C. A. Pignedoli, K. Müllen, R. Fasel, X. Feng, P. Ruffieux, *J. Am. Chem. Soc*. **2019**, *141*, 10621, https://doi.org/10.1021/jacs.9b05319.
[16] S. Mishra, J. Melidonie, K. Eimre, S. Obermann, O. Gröning, C. A. Pignedoli, P. Ruffieux, X. Feng, R. Fasel, *Chem. Commun*. **2020**, https://doi.org/10.1039/D0CC02513E.
[17] S. Mishra, X. Yao, Q. Chen, K. Eimre, O. Gröning, R. Ortiz, M. Di Giovannantonio, J. C. Sancho-García, J. Fernández-Rossier, C. A. Pignedoli, K. Müllen, P. Ruffieux, A. Narita, R. Fasel, *Nat. Chem*. **2021**, *13*, 581, https://doi.org/10.1038/s41557-021-00678-2.
[18] J. Su, W. Fan, P. Mutombo, X. Peng, S. Song, M. Ondráček, P. Golub, J. Brabec, L. Veis, M. Telychko, P. Jelínek, J. Wu, J. Lu, *Nano Lett*. **2021**, *21*, 861, https://doi.org/10.1021/acs.nanolett.0c04627.
[19] S. Mishra, G. Catarina, F. Wu, R. Ortiz, D. Jacob, K. Eimre, J. Ma, C. A. Pignedoli, X. Feng, P. Ruffieux, J. Fernández-Rossier, R. Fasel, *Nature* **2021**, *598*, 287, https://doi.org/10.1038/s41586-021-03842-3.
[20] M. Bieri, M.-T. Nguyen, O. Gröning, J. Cai, M. Treier, K. Aït-Mansour, P. Ruffieux, C. A. Pignedoli, D. Passerone, M. Kastler, K. Müllen, R. Fasel, *J. Am. Chem. Soc*. **2010**, *132*, 16669, https://doi.org/10.1021/ja107947z.
[21] C. Steiner, J. Gebhardt, M. Ammon, Z. Yang, A. Heidenreich, N. Hammer, A. Görling, M. Kivala, S. Maier, *Nat. Commun*. **2017**, *8*, 14765, https://doi.org/10.1038/ncomms14765.
[22] G. Galeotti, F. De Marchi, E. Hamzehpoor, O. MacLean, M. Rajeswara Rao, Y. Chen, L. V. Besteiro, D. Dettmann, L. Ferrari, F. Frezza, P. M. Sheverdyaeva, R. Liu, A. K. Kundu, P. Moras, M. Ebrahimi, M. C. Gallagher, F. Rosei, D. F. Perepichka, G. Contini, *Nat. Mater*. **2020**, *1*, https://doi.org/10.1038/s41563-020-0682-z.
[23] M. Di Giovannantonio, G. Contini, *J. Phys. Condens. Matter* **2018**, *30*, 093001, https://doi.org/10.1088/1361-648X/aaa8cb.
[24] L. Gross, F. Mohn, N. Moll, P. Liljeroth, G. Meyer, *Science* **2009**, *325*, 1110, https://doi.org/10.1126/science.1176210.
[25] L. Gross, F. Mohn, N. Moll, B. Schuler, A. Criado, E. Guitián, D. Peña, A. Gourdon, G. Meyer, *Science* **2012**, *337*, 1326, https://doi.org/10.1126/science.1225621.
[26] K. Bian, C. Gerber, A. J. Heinrich, D. J. Müller, S. Scheuring, Y. Jiang, *Nat. Rev. Methods Primer* **2021**, *1*, 1, https://doi.org/10.1038/s43586-021-00033-2.
[27] D. A. King, *Surf. Sci*. **1975**, *47*, 384.
[28] S. Dutta, A. J. Gellman, *Chem. Soc. Rev*. **2017**, *46*, 7787, https://doi.org/10.1039/c7cs00555e.
[29] M. Di Giovannantonio, O. Deniz, J. I. Urgel, R. Widmer, T. Dienel, S. Stolz, C. Sánchez-Sánchez, M. Muntwiler, T. Dumslaff, R. Berger, A. Narita, X. Feng, K. Müllen, P. Ruffieux, R. Fasel, *ACS Nano* **2018**, *12*, 74, https://doi.org/10.1021/acsnano.7b07077.
[30] R. Larciprete, S. Fabris, T. Sun, P. Lacovig, A. Baraldi, S. Lizzit, *J. Am. Chem. Soc*. **2011**, *133*, 17315, https://doi.org/10.1021/ja205168x.
[31] M. Di Giovannantonio, M. El Garah, J. Lipton-Duffin, V. Meunier, L. Cardenas, Y. Fagot Revurat, A. Cossaro, A. Verdini, D. F. Perepichka, F. Rosei, G. Contini, *ACS Nano* **2013**, *7*, 8190, https://doi.org/10.1021/nn4035684.
[32] K. A. Simonov, N. A. Vinogradov, A. S. Vinogradov, A. V. Generalov, E. M. Zagrebina, N. Mårtensson, A. A. Cafolla, T. Carpy, J. P. Cunniffe, A. B. Preobrajenski, *J. Phys. Chem. C* **2014**, *118*, 12532, https://doi.org/10.1021/jp502215m.
[33] K. A. Simonov, N. A. Vinogradov, A. S. Vinogradov, A. V. Generalov, E. M. Zagrebina, G. I. Svirskiy, A. A. Cafolla, T. Carpy, J. P. Cunniffe, T. Taketsugu, A. Lyalin, N. Mårtensson, A. B. Preobrajenski, *ACS Nano* **2015**, *9*, 8997, https://doi.org/10.1021/acsnano.5b03280.
[34] M. Di Giovannantonio, M. Tomellini, J. Lipton-Duffin, G. Galeotti, M. Ebrahimi, A. Cossaro, A. Verdini, N. Kharche, V. Meunier, G. Vasseur, Y. Fagot-Revurat, D. F. Perepichka, F. Rosei, G. Contini, *J. Am. Chem. Soc*. **2016**, *138*, 16696, https://doi.org/10.1021/jacs.6b09728.
[35] G. Galeotti, M. Di Giovannantonio, J. Lipton-Duffin, M. Ebrahimi, S. Tebi, A. Verdini, L. Floreano, Y. Fagot-Revurat, D. F. Perepichka, F. Rosei, G. Contini, *Faraday Discuss*. **2017**, *204*, 453, https://doi.org/10.1039/C7FD00099E.
[36] M. Fritton, D. A. Duncan, P. S. Deimel, A. Rastgoo-Lahrood, F. Allegretti, J. V. Barth, W. M. Heckl, J. Björk, M. Lackinger, *J. Am. Chem. Soc*. **2019**, *141*, 4824, https://doi.org/10.1021/jacs.8b11473.
[37] J. Fester, Z. Sun, J. Rodríguez-Fernández, A. S. Walton, J. V. Lauritsen, *J. Phys. Chem. C* **2019**, *123*, 9176, https://doi.org/10.1021/acs.jpcc.9b00771.
[38] G. Galeotti, M. Di Giovannantonio, A. Cupo, S. Xing, J. Lipton-Duffin, M. Ebrahimi, G. Vasseur, B. Kierren, Y. Fagot-Revurat, D. Tristant, V. Meunier, D. F. Perepichka, F. Rosei, G. Contini, *Nanoscale* **2019**, *11*, 7682, https://doi.org/10.1039/C9NR00672A.
[39] C. J. (Kees-J. Weststrate, D. Sharma, D. Garcia Rodriguez, M. A. Gleeson, H. O. A. Fredriksson, J. W. (Hans) Niemantsverdriet, *Nat. Commun*. **2020**, *11*, 750, https://doi.org/10.1038/s41467-020-14613-5.
[40] M. Abadia, G. Vasseur, M. Kolmer, L. Zajac, A. Verdini, J. E. Ortega, L. Floreano, C. Rogero, J. Brede, *J. Phys. Chem. C* **2020**, *124*, 16918, https://doi.org/10.1021/acs.jpcc.0c02125.
[41] J. I. Urgel, M. D. Giovannantonio, K. Eimre, T. G. Lohr, J. Liu, S. Mishra, Q. Sun, A. Kinikar, R. Widmer, S. Stolz, M. Bommert, R. Berger, P. Ruffieux, C. A. Pignedoli, K. Müllen, X. Feng, R. Fasel, *Angew. Chem.* **2020**, *132*, 13383, https://doi.org/10.1002/ange.202001939.
[42] S. Stolz, M. Di Giovannantonio, J. I. Urgel, Q. Sun, A. Kinikar, G. Borin Barin, M. Bommert, R. Fasel, R. Widmer, *Angew. Chem. Int. Ed.* **2020**, *59*, 14106, https://doi.org/10.1002/anie.202005443.
[43] S. Stolz, M. Danese, M. Di Giovannantonio, J. I. Urgel, Q. Sun, A. Kinikar, M. Bommert, S. Mishra, H. Brune, O. Gröning, D. Passerone, R. Widmer, *Adv. Mater*. **2022**, *34*, 2104481, https://doi.org/10.1002/adma.202104481.
[44] A. Berdonces-Layunta, F. Schulz, F. Aguilar-Galindo, J. Lawrence, M. S. G. Mohammed, M. Muntwiler, J. Lobo-Checa, P. Liljeroth, D. G. de Oteyza, *ACS Nano* **2021**, https://doi.org/10.1021/acsnano.1c06226.
[45] G. Borin Barin, Q. Sun, M. Di Giovannantonio, C.-Z. Du, X.-Y. Wang, J. P. Llinas, J. Wilhelm, J. Overbeck, C. Daniels, M. Lamparski, H. Sahabudeen, M. L. Perrin, J. I. Urgel, S. Mishra, A. Kinikar, R. Widmer, S. Stolz, M. Bommert, C. A. Pignedoli, X. Feng, M. Calame, V. Meunier, J. Bokor, A. Narita, K. Müllen, R. Fasel, P. Ruffieux, *arxiv*: 2202.0110.
[46] D. Dettmann, G. Galeotti, O. MacLean, M. Tomellini, M. Di Giovannantonio, J. Lipton-Duffin, A. Verdini, L. Floreano, Y. Fagot-Revurat, D. F. Perepichka, F. Rosei, G. Contini, *Small* **2021**, *17*, 2103044, https://doi.org/10.1002/smll.202103044.
[47] Molecular Lego: Bottom-up Fabrication of Atomically Precise Graphene Nanostructures (37), https://www.sps.ch/en/artikel/progresses/molecular-lego-bottom-up-fabrication-of-atomically-precise-graphene-nanostructures-37, accessed November 23, 2021.
[48] L. Talirz, H. Söde, T. Dumslaff, S. Wang, J. R. Sanchez-Valencia, J. Liu, P. Shinde, C. A. Pignedoli, L. Liang, V. Meunier, N. C. Plumb, M. Shi, X. Feng, A. Narita, K. Müllen, R. Fasel, P. Ruffieux, *ACS Nano* **2017**, *11*, 1380, https://doi.org/10.1021/acsnano.6b06405.
[49] C. Papp, H.-P. Steinrück, *Surf. Sci. Rep*. **2013**, *68*, 446, https://doi.org/10.1016/j.surfrep.2013.10.003.
[50] M. Muntwiler, J. Zhang, R. Stania, F. Matsui, P. Oberta, U. Flechsig, L. Patthey, C. Quitmann, T. Glatzel, R. Widmer, E. Meyer, T. A. Jung, P. Aebi, R. Fasel, T. Greber, *J. Synchrotron Radiat*. **2017**, *24*, 354, https://doi.org/10.1107/S1600577516018646.
[51] W. Wang, X. Shi, S. Wang, M. A. Van Hove, N. Lin, *J. Am. Chem. Soc*. **2011**, *133*, 13264, https://doi.org/10.1021/ja204956b.
[52] B. Yuan, C. Li, Y. Zhao, O. Gröning, X. Zhou, P. Zhang, D. Guan, Y. Li, H. Zheng, C. Liu, Y. Mai, P. Liu, W. Ji, J. Jia, S. Wang, *J. Am. Chem. Soc*. **2020**, *142*, 10034, https://doi.org/10.1021/jacs.0c01930.

[53] S. J. Blanksby, G. B. Ellison, *Acc. Chem. Res*. **2003**, *36*, 255, https://doi.org/10.1021/ar020230d.
[54] J. Björk, F. Hanke, S. Stafström, *J. Am. Chem. Soc*. **2013**, *135*, 5768, https://doi.org/10.1021/ja400304b.
[55] L. Martini, Z. Chen, N. Mishra, G. B. Barin, P. Fantuzzi, P. Ruffieux, R. Fasel, X. Feng, A. Narita, C. Coletti, K. Müllen, A. Candini, *Carbon* **2019**, *146*, 36, https://doi.org/10.1016/j.carbon.2019.01.071.
[56] Z. Xiao, C. Ma, W. Lu, J. Huang, L. Liang, K. Hong, A.-P. Li, B. G. Sumpter, J. Bernholc, *Npj Comput. Mater*. **2019**, *5*, 91, https://doi.org/10.1038/s41524-019-0228-6.
[57] C. Ma, Z. Xiao, P. V. Bonnesen, L. Liang, A. A. Puretzky, J. Huang, M. Kolmer, B. G. Sumpter, W. Lu, K. Hong, J. Bernholc, A.-P. Li, *Chem. Sci*. **2021**, *12*, 15637, https://doi.org/10.1039/D1SC04908A.
[58] M. Abyazisani, J. M. MacLeod, J. Lipton-Duffin, *ACS Nano* **2019**, *13*, 9270, https://doi.org/10.1021/acsnano.9b03812.
[59] A. Kimouche, M. M. Ervasti, R. Drost, S. Halonen, A. Harju, P. M. Joensuu, J. Sainio, P. Liljeroth, *Nat. Commun*. **2015**, *6*, 10177, https://doi.org/10.1038/ncomms10177.
[60] S. W. Smith, *Toxicol. Sci. Off. J. Soc. Toxicol*. **2009**, *110*, 4, https://doi.org/10.1093/toxsci/kfp097.
[61] B. Kasprzyk-Hordern, *Chem. Soc. Rev*. **2010**, *39*, 4466, https://doi.org/10.1039/C000408C.
[62] D. Rosenthal, R. Widmer, R. Wagner, P. Gille, M. Armbrüster, Y. Grin, R. Schlögl, O. Gröning, *Langmuir* **2012**, *28*, 6848, https://doi.org/10.1021/la2050509.
[63] J. Prinz, R. Gaspari, C. A. Pignedoli, J. Vogt, P. Gille, M. Armbrüster, H. Brune, O. Gröning, D. Passerone, R. Widmer, *Angew. Chem*. **2012**, *124*, 9473, https://doi.org/10.1002/ange.201203787.
[64] C. Sanchez-Sanchez, N. Orozco, J. P. Holgado, S. K. Beaumont, G. Kyriakou, D. J. Watson, A. R. Gonzalez-Elipe, L. Feria, J. Fernández Sanz, R. M. Lambert, *J. Am. Chem. Soc*. **2015**, *137*, 940, https://doi.org/10.1021/ja5115584.
[65] R. Zhang, G. Lyu, D. Y. Li, P. N. Liu, N. Lin, *Chem. Commun.* **2017**, *53*, 1731, https://doi.org/10.1039/C6CC10091K.
[66] K.-J. Shi, C.-H. Shu, C.-X. Wang, X.-Y. Wu, H. Tian, P.-N. Liu, *Org. Lett*. **2017**, *19*, 2801, https://doi.org/10.1021/acs.orglett.7b00855.
[67] W. M. H. Sachtler, *Catal. Rev. - Sci. Eng*. **1976**, *14*, 193, https://doi.org/10.1080/03602457608073411.